Faraday Discussions

Accepted Manuscript

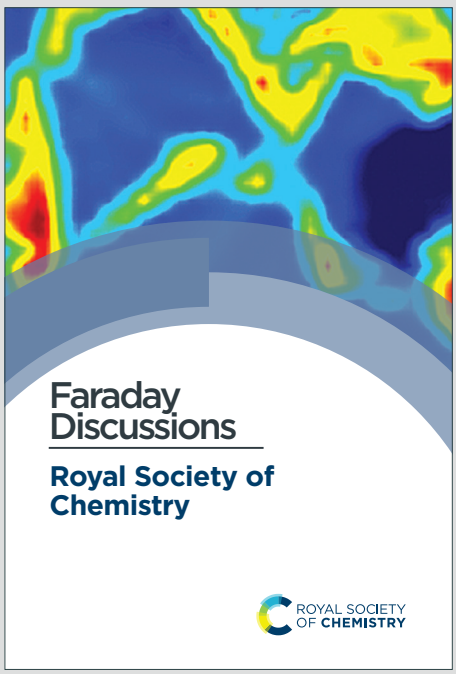

This article can be cited before page numbers have been issued, to do this please use: Z. Rehman, J. Lubay, W. T. T. Franks, E. Corlett, B. Nguyen, G. Scrivens, B. Samas, H. Frericks-Schmidt and S. P. Brown, *Faraday Discuss.*, 2024, DOI: 10.1039/D4FD00088A.

ROYAL SOCIETY OF CHEMISTRY

www.rsc.org/faraday_d

Organic NMR Crystallography: Enabling Progress for Applications to Pharmaceuticals and Plant Cell Walls

View Article Online
DOI: 10.1039/D4FD00088A

Zainab Rehman,[a] Jairah Lubay,[a] W. Trent Franks,[a] Emily K. Corlett,[b] Bao Nguyen,[c] Garry Scrivens,[b] Brian M. Samas,[c] Heather Frericks-Schmidt,[c] and Steven P. Brown[a]*

a Department of Physics, University of Warwick, Coventry, CV4 7AL, UK.
b Pfizer Worldwide R&D, Sandwich, Kent, UK.
c Pfizer Worldwide R&D, Groton, CT, USA.
*E-mail: S.P.Brown@warwick.ac.uk

Keywords: DFT; GIPAW; NMR; chemical shift; electric field gradient; ^{1}H; ^{13}C; ^{14}N; ^{15}N; pharmaceuticals; cellulose

Abstract

The application of NMR crystallography to organic molecules is exemplified by two case studies. For the tosylate salt of the active pharmaceutical ingredient, Ritlectinib, solid-state NMR spectra are presented at a ^{1}H Larmor frequency of 1 GHz and a magic-angle spinning (MAS) frequency of 60 kHz. Specifically, ^{14}N-^{1}H heteronuclear multiple-quantum coherence (HMQC) and ^{1}H-^{1}H double-quantum (DQ) single-quantum (SQ) correlation experiments are powerful probes of hydrogen bonding interactions. A full assignment of the ^{1}H, ^{13}C and ^{14}N/^{15}N chemical shifts is achieved using also ^{1}H-^{13}C cross polarization (CP) HETCOR spectra together with gauge-including projector augmented wave (GIPAW) DFT calculation for the geometry-optimised X-ray diffraction crystal structure that is reported here (CCDC 2352028). In addition, GIPAW calculations are presented for the ^{13}C chemical shifts in the two polymorphs of cellulose for which diffraction structures are available. For both case studies, a focus is on the discrepancy between experiment and GIPAW calculation.

Introduction

Built upon the DFT gauge-including projector augmented wave (GIPAW) method,[1-3] the value of NMR crystallography for analysis of solid-state structures of organic molecules is being increasingly recognised. This paper aims to take stock of where the field is today, notably considering that experimental solid-state NMR can now readily access magnetic fields corresponding to a ^{1}H Larmor frequency of at least 1 GHz and magic-angle spinning (MAS)

frequencies of at least 60 kHz. The paper identifies current challenges and points to new approaches under consideration. The focus is on applications to pharmaceuticals,[4] but suitability for aiding in the interpretation of solid-state NMR spectra of plant cell walls[5] is also considered.

For the calculation of chemical shieldings for the spin $I = 1/2$ nuclei ^{1}H and ^{13}C, there is an extensive literature that the collaborative computational project for NMR crystallography (CCP-NC) database[6] based on the .magres format[7] is endeavouring to bring into one place. From this extensive literature, it is well established that the discrepancy with respect to experiment is usually within 1% of the chemical shift range, i.e., within ~0.2 ppm and ~2 ppm for ^{1}H and ^{13}C chemical shifts, respectively.[3,8,9]

That said, there are challenges. It is known that the gradient of a plot of experimental isotropic chemical shift against GIPAW calculated absolute shielding deviates from minus one,[10] and there is disagreement in the community as to how referencing should be carried out. It is to be noted that this referencing problem is circumvented by a recently published method that considers differences in calculated chemical shielding between solution and the solid state. Such a difference does not require referencing, and an evaluation of correlation with respect to the corresponding change in experimental chemical shift between solution and solid enables the differentiation of solid-state form.[11,12] We also note that larger discrepancies between experiment and GIPAW calculation have been systematically observed for specific chemical groups, notably for OH…O ^{1}H and N=C-N ^{13}C chemical shifts.[13] Moreover, there remains the challenge that GIPAW calculation at an effective temperature of 0 K does not reproduce the known temperature dependence of hydrogen-bonded ^{1}H chemical shifts.[14-17] An important quadrupolar ($I \geq 1$) nucleus for studying hydrogen bonding interactions in organic solids is ^{14}N for which ^{1}H detection is important;[18-22] DFT calculation is valuable for prediction of the electric field gradients that determines the quadrupolar parameters that affect the solid-state NMR spectra.

A Review of Applications of NMR crystallography to Pharmaceutical Molecules

As one of the fathers of the field of NMR crystallography, alongside Francis Taulelle,[23] Robin Harris focused on applications to small and moderately sized organic molecules, notably, pharmaceuticals.[24,25] Early applications of the GIPAW method were, with Chris Pickard, Francesco Mauri and Jonathan Yates, for the calculation of ^{1}H, ^{13}C and ^{19}F chemical shifts in the pharmaceutical, flurbiprofen, presented with MAS NMR spectra,[26] and, together with Lyndon Emsley, for the calculation of ^{13}C chemical shifts for testosterone for the two distinct

View Article Online
DOI: 10.1039/D4FD00088A

molecules in the asymmetric unit cell, presented with two-dimensional ^{13}C refocused INADEQUATE MAS NMR spectra.[27]

Applications to pharmaceuticals up to 2018 are referred to in the comprehensive review of NMR crystallography of organic solids by Hodgkinson;[9] here, we refer to some specific highlights. The added value of an NMR crystallography approach for quantifying intermolecular interactions, notably hydrogen bonding, was demonstrated by calculations of the change in chemical shift between a GIPAW calculation for the full crystal structure and an isolated molecule for phenylphosponic acid by Gervais et al.,[28] for maltose anomers by Yates et al.,[29] and by Bradley et al. for the pharmaceutical indomethacin.[30] A significant advance was the coupling of NMR crystallography with crystal structure prediction (CSP) by Emsley and Day and co-workers, whereby, as demonstrated for thymol, best agreement to the putative CSP structures was obtained via determining the root mean squared error (RMSE) between experimental and GIPAW calculated ^{1}H and ^{13}C chemical shifts.[31] The importance of NMR crystallography to the pharmaceutical industry is demonstrated by a growing number of publications in collaboration with scientists from pharmaceutical companies, for example to sibenadet polymorphs with AstraZeneca[32] and to cimetidine and tenoxicam with GlaxoSmithKline,[33] both in 2012. The potential to incorporate dispersion correction into DFT calculations in the DFT-D approach was demonstrated by Dudenko et al. for indomethacin in 2013.[34] As an alternative to the GIPAW planewave method, Beran and co-workers have advocated for a fragment-based approach that permit the use of hybrid functionals such as PBE0.[35-38] A major advance whose significance is ever increasing was the development in 2018 by Ceriotti, Emsley and co-workers of the Shift-ML method for predicting chemical shifts by applying machine learning based on a training set of GIPAW calculated chemical shifts.[39]

Focusing on the last five years since 2019, there have been a range of impressive applications of NMR crystallography and methodological advances. Combining NMR crystallography, including two-dimensional ^{1}H-^{13}C and ^{1}H-^{15}N HETCOR MAS NMR spectra, with electron diffraction, Guzman-Alfonso have identified the hydrogen bonding network in form B of the pharmaceutical, cimetidine.[40] Bartova et al. have combined calculation with experiment, notably ^{14}N-^{1}H two-dimensional MAS NMR spectra, to study tautomerism in azo dyes, focusing on hydrogen bonding interactions.[41] Scarperi et al. have used NMR crystallography to study the pharmaceutical carbimazole, presenting ^{1}H DQ and ^{1}H-^{13}C heteronuclear correlation MAS NMR spectra.[42] Dudek et al. have used NMR crystallography with ^{1}H DQ MAS NMR spectra to probe the co-crystal landscape when an AB binary system (barbituric acid: thiobarbituric acid) is perturbed by a crystalline synthon C (1-hydroxy-4,5-dimethyl-

imidazole 3-oxide) in a ball mill.[43] Dudek and co-workers and Pawlak et al have also combined NMR crystallography with CSP for co-crystals of the antibiotic linezolid[44] and for the pharmaceutical teriflunomide.[45] Mathew et al. have presented an NMR crystallography study of the pharmaceutical sitagliptin phosphate monohydrate including ^{13}C-^{13}C and ^{13}C-^{15}N MAS NMR correlation spectra recorded at natural abundance using dynamic nuclear polarisation.[46] Brouwer and Mikolajewski have recently presented GIPAW calculations along with ^{1}H DQ and ^{1}H-^{13}C heteronuclear correlation MAS NMR spectra for glucose, to identify trends in the ^{1}H chemical shift with hydrogen bonding parameters,[47] noting that Shen et al. have presented GIPAW calculations to complement ^{17}O MAS NMR experiments for the same sugar molecule.[48] Chierotti and co-workers have combined experiment such as ^{1}H DQ and ^{1}H-^{13}C heteronuclear correlation as well as ^{14}N-^{1}H MAS NMR spectra, and GIPAW calculation to study co-crystals of the pharmaceutical ethionamide,[49] probe tautomerism in the pharmaceutical mebanazole,[50] identify zwitterions, in combination with CSP, in isomers of pyridine dicarboxylic acid,[51] and to analyse leucopterin, the white pigment in butterfly wings, including a ^{1}H DQ MAS spectrum at 1 GHz.[52] Working together with scientists at AstraZeneca and Pfizer, Brown and co-workers have presented NMR crystallography studies of a range of pharmaceutical molecules.[4,33,53-56]

Together with Dracinsky, Hodgkinson has advocated for bringing together of molecular dynamics and nuclear quantum effects in the path-integral molecular dynamics (PIMD) approach.[57] This proves important for predicting salt or co-crystal formation corresponding to the transfer or not of a proton, as evidenced by the ^{1}H chemical shift.[58,59] Dracinsky has investigated geometry optimisation using the hybrid functional B3LYP or the meta-GGA functional rSCAN[60] and observe improved agreement compared to experiment for ^{1}H chemical shifts, though there is not clear improvement for ^{13}C chemical shifts.[61] This analysis has been extended to NMR crystallography of amino acids.[62] Recently, building upon the use of a molecular correction term with a hybrid density functional,[63] Iulucci et al. have compared the agreement compared to experiment for computationally more expensive double hybrid or Moller-Plesset perturbation theory (MP2), with no advantage for the test set of ^{13}C and ^{15}N chemical shifts being observed.[64] Schurko and co-workers have investigated how hybrid density functionals can improve agreement with respect to experiment for the ^{13}C chemical shielding tensor for the pharmaceutical cimetidine.[65] Recently Holmes et al. have compared the agreement to experiment for the ^{13}C chemical shielding tensor for five nitrogen-dense compounds when employing the hybrid functional PBE0 or the double-hybrid functional PBE0-DH.[66] Emsley and co-workers have published a series of impressive papers that make

use of the ShiftML resource. Bayesian statistical theory has been integrated into the use of NMR chemical shifts, [67,68] and to enhance crystal structure prediction protocols.[69,70] Chemical-shift dependent interaction maps based on ShiftML have been presented.[71] Working with scientists at AstraZeneca, structural insight has been derived for amorphous pharmaceuticals.[72,73]

Experimental and Computational Details

Solid-State NMR

Experiments were performed using a Bruker Avance III, a Bruker Avance II+, and a Bruker NEO spectrometer operating at a ^{1}H Larmor frequency of 500.0 MHz, 600.0 MHz, and 1000.0 MHz, respectively, corresponding to a ^{13}C Larmor frequency of 125.8 MHz, 150.9 MHz, and 251.5 MHz, respectively. ^{14}N-^{1}H experiments were performed at a ^{1}H Larmor frequency of 600 MHz and a ^{14}N Larmor frequency of 43.4 MHz. A 1.3 mm HXY probe at 60 kHz MAS and a 4 mm HXY probe at 12.5 kHz MAS, both in double resonance mode, were utilised. The ^{1}H 90° pulse duration was 2.5 µs corresponding to a ^{1}H nutation frequency of 100 kHz. SPINAL-64 ^{1}H heteronuclear decoupling[74] was employed during the acquisition of a ^{13}C or ^{15}N FID. In all 2D experiments, States-TPPI was used to obtain sign-discrimination in F_1. A recycle delay of 12 s was used.

^{1}H-^{13}C 1D Cross-Polarisation (CP) MAS NMR and 2D CP Heteronuclear Correlation (HETCOR) MAS NMR at 600 MHz and 1 GHz. For CP at 12.5 kHz MAS, CP was achieved using a ramp (70-100%).[75] The nutation frequencies for ^{1}H and ^{13}C, respectively, during CP were approximately 100 kHz and 80 kHz at 600 MHz and 12.5 kHz MAS and 50 kHz and 10 kHz at 1 GHz and 60 kHz MAS. The SPINAL-64 pulse duration was 5.1 µs at 12.5 kHz MAS and 45.8 µs at 60 kHz MAS. The phase cycling employed was as follows: ^{1}H 90° pulse (90° 270°), ^{13}C CP contact pulse (2{0°} 2{180°} 2{90°} 2{270°}), receiver (0° 180° 180° 0° 90° 270° 270 °90°).

For HETCOR at 1 GHz and 60 kHz MAS, no homonuclear ^{1}H decoupling was applied in t_1. 1 GHz spectra were recorded with low-power ^{13}C rf. irradiation during CP at an irradiation frequency of 50 ppm or 120 ppm. Here, 32 transients were co-added for each of the 128 (^{13}C at 120 ppm) or 192 (^{13}C at 50 ppm) t_1 FIDs using a t_1 increment of 50 µs, resulting in an experimental time of 14 or 21 hours.

^{1}H-^{15}N 1D Cross-Polarisation (CP) MAS NMR. CP was achieved using a ramp on ^{1}H (50-100%),[75] with the same phase cycling as for the ^{1}H-^{13}C experiments. The nutation frequencies

View Article Online
DOI: 10.1039/D4FD00088A

for ^{1}H and ^{15}N during CP were 70 kHz and 25 kHz. The SPINAL-64 pulse duration was 5.3 μs at a ^{1}H nutation frequency of 100 kHz.

Fast MAS (60 kHz) ^{1}H-^{1}H 2D NMR Experiments at 600 MHz and 1 GHz. ^{1}H-^{1}H double quantum (DQ) spectra with one rotor period of BaBa recoupling[76,77] were acquired using a rotor-synchronised t_1 increment of 16.67 μs. In both cases, 48 transients were co-added for each of the 128 t_1 FIDs, corresponding to an experimental time of 21 hours. A 16-step phase cycle was implemented, with $\Delta p = \pm 2$ selected during DQ excitation (4 steps) and $\Delta p = -1$ on the *z*-filter 90° pulse (4 steps), where p is the coherence order. The phase cycling employed was as follows: ^{1}H BABA pulses (0° 90° 180° 270°), ^{1}H 90° (*z*-filter) (4 {0°} 4{90°} 4{180°} 4{270°}), receiver (0° 180° 0° 180° 90° 270° 90° 270° 180° 0° 180° 0° 270° 90° 270° 90°).

2D ^{14}N-^{1}H HMQC[18-22] MAS (60 kHz) NMR Experiments. These were acquired with 8 rotor periods (133.6 μs), 16 rotor periods (267.2 μs) and 24 rotor periods (400.8 μs) of phase-inverted R^3 recoupling with $+x\ -x$ phase inversion for every rotor period of the $n = 2$ ($\nu_1 = 2\nu_R$) rotary resonance recoupling pulses.[19,22,78-81] A rotor-synchronised t_1 increment of 16.67 μs was used. The experiments were obtained with 32 coadded transients for each of the 256 t_1 FIDs, corresponding to 27 hours experimental time. A 4-step nested phase cycle was used to select changes in the coherence order $\Delta p = \pm 1$ on the first ^{1}H pulse (2 steps) and $\Delta p = \pm 1$ on the last ^{14}N pulse (2 steps).

Referencing. The ^{13}C and ^{1}H chemical shifts were referenced with respect to tetramethylsilane (TMS) using L-alanine at natural abundance as the secondary reference. The CH_3 group of L-alanine is referenced at 1.1 ppm for the ^{1}H methyl resonance and 177.8 ppm for the ^{13}C carboxylate resonance. This corresponds to adamantane at 1.85 ppm for ^{1}H[82] and 38.5 ppm for ^{13}C.[83] The ^{14}N shifts were referenced with respect to saturated NH_4Cl aqueous solution using β-aspartyl-L-alanine at natural abundance, whereby the NH resonance is at –284 ppm at a ^{1}H Larmor frequency of 600 MHz, corresponding to liquid CH_3NO_2 at 0 ppm.[21,84] The ^{15}N chemical shifts are also referenced to liquid CH_3NO_2 at 0 ppm.[85] For equivalence to the chemical shift scale frequently used in protein ^{15}N NMR, where the alternative IUPAC reference (see Appendix 1 of ref[86]) is liquid ammonia at 50 °C, it is necessary to add 379.5 ppm to the given values.[87] The accuracy of the experimental shifts is within ±0.2, ±0.1 and ±5 for ^{1}H, ^{13}C and ^{15}N, and ^{14}N, respectively.

GIPAW Calculations

Density functional theory (DFT) calculations were performed using CASTEP[88] version 19.1 for **1** and version 20.1 for the cellulose polymorphs. For the full crystal, geometry optimisation with fixed unit cell parameters followed by magnetic shielding calculations to determine the NMR parameters were completed. Distances stated in this paper are for the geometry optimised crystal structure. The Perdew Burke Ernzerhof (PBE) exchange correlation functional,[89] a plane-wave basis set with ultrasoft pseudopotentials and a plane-wave cut-off energy of 800 eV were implemented. A minimum Monkhorst-Pack grid spacing of 2π x 0.1 $Å^{-1}$ was used. The GIPAW[1,2] method was used to calculate the NMR parameters: calculated isotropic chemical shifts were determined from the calculated chemical shieldings according to $\delta_{iso\_calc} = \sigma_{ref} - \sigma_{calc}$. It is noted that it is common practice to calculate a specific reference shielding for each system (see, e.g., Table S8 of ref.[39]), though average values over a range of compounds are also available.[38] For **1**, ^{13}C, different reference shieldings were used for high- and low ppm chemical shifts:[90] 172 ppm for > 45 ppm and 175 ppm for < 45 ppm. For **2**, a reference shielding of 168 ppm was used. For ^{1}H and ^{15}N, a reference shielding of 31 ppm and −160 ppm was used, respectively.

Case Study 1: The Active Pharmaceutical Ingredient Ritlectinib Tosylate

This section showcases current state-of-the-art experimental solid-state NMR for the application of NMR crystallography to moderately sized active pharmaceutical ingredients (APIs). The API, Ritlecitinib,[91] functions as a selective and irreversible JAK3 inhibitor for irritable bowel disease with additional studies in progress for further uses as a treatment for alopecia areata[92] and Crohn's disease.[93] The irreversible binding is covalent in nature to a specific Cysteine residue (Cys-909) within the JAK3 protein.[94] The original synthesis for the molecule, Ritlectinib, was described by Thorarensen et al.[95] In this work, the API is considered in its tosylate salt form, **1** (see Scheme 1).[96]

View Article Online
DOI: 10.1039/D4FD00088A

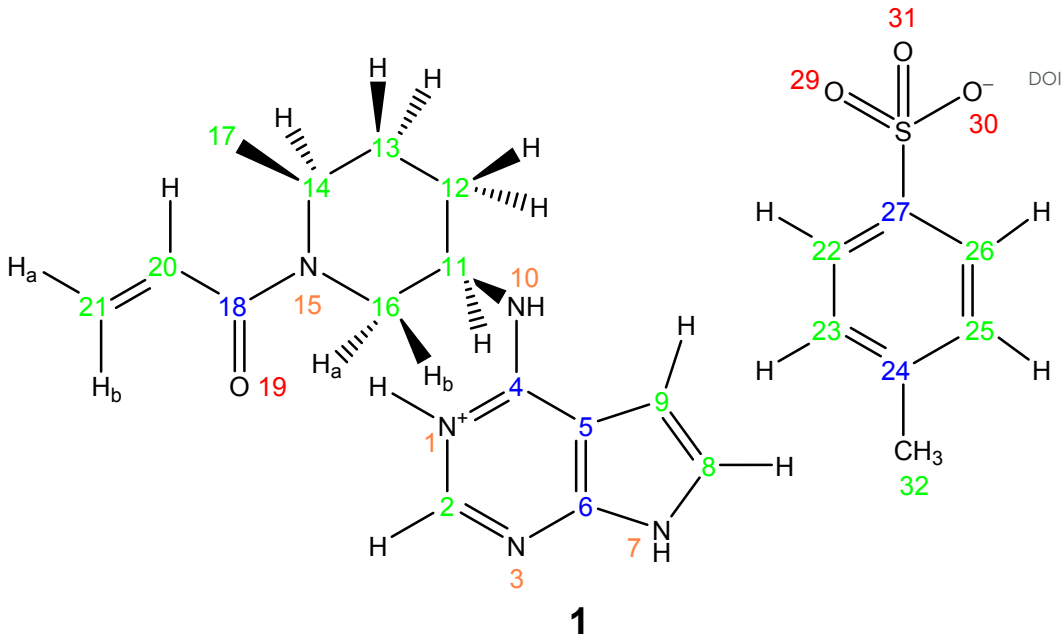

1

Scheme 1.

NMR crystallography is particularly well suited to the probing of intermolecular hydrogen bonding that is a key driver of the specific crystal packing adopted in the solid state. Advantage is taken of the marked sensitivity of the ^{1}H chemical shift and also the ^{14}N/ ^{15}N chemical shift and the ^{14}N quadrupolar interaction to hydrogen bonding.[22,33,97,98] This is illustrated for **1** in Figure 1 that presents a two-dimensional ^{14}N-^{1}H heteronuclear multiple-quantum coherence (HMQC)[18-22] (Figure 1a) and a ^{1}H-^{15}N cross polarization (CP) (Figure 1b) MAS NMR spectrum. Note that there are two NMR-active nuclei for nitrogen, ^{14}N and ^{15}N, with natural abundances of 99.6% and 0.4%, respectively, whereby the ^{15}N nucleus has spin $I = 1/2$, while the ^{14}N nucleus has spin $I = 1$. The NMR spectra of nuclei with $I \geq 1$ are affected by strong quadrupolar interactions between the electric quadrupole moment of the nucleus and the surrounding electric field gradient.

In Figure 1a, intense ^{14}N-^{1}H correlation peaks are observed at a ^{1}H chemical shift of 12.8 and 13.6 ppm for a ^{14}N shift of –46 and –40 ppm, respectively, that are assigned (see below discussion) to the N7-H7 and N1-H1 directly bonded pairs of dipolar-coupled nuclei. As illustrated in Figure 1 by the double-headed arrows, this corresponds to a change as compared to the ^{15}N chemical shifts observed in Figure 1b of 187 and 183 ppm, respectively. This difference arises because the ^{14}N shift is the sum of the isotropic chemical shift (that to a good approximation is the same for ^{14}N and ^{15}N) and the isotropic second-order quadrupolar shift whose magnitude depends on the strength of the quadrupolar interaction (and is also inversely

proportional to the B_0 magnetic field).[21] The assignment of the observed peaks is made on the basis of a DFT calculation using the GIPAW method as implemented within the CASTEP program. By taking as input a DFT geometry-optimised crystal structure of **1**, the GIPAW calculation yields the chemical shielding and the electric field gradient for each nucleus both of which depend on the electronic environment. Table 1 lists the experimental and GIPAW calculated ^{14}N and ^{15}N NMR parameters for **1**. It is observed that the experimental quadrupolar product is the same for N1 and N7 at 2.5 MHz which is ~20% bigger than the calculated magnitudes of 2.2 and 2.1 MHz, respectively.

Lower intensity peaks are also observed at a ^{1}H chemical shift of 9.2 ppm that corresponds to the H10 atom that is directly bonded to the N10. The peak at a ^{14}N shift of –40 ppm corresponds to a longer range N…H proximity between N10 and H1 that is bonded to the neighbouring N1 atom in the six-membered aromatic ring. The observation of this correlation peak enables the assignment of the N1-H1 cross peak, that is not possible based on the GIPAW calculation of the nitrogen chemical shift. Note that the calculated values of N1 and N7 are within 0.1 ppm, whereas the experimental ^{15}N chemical shifts differ by 8.8 ppm (see Table 1). A low intensity N10-H10 correlation peak is observed at a ^{14}N shift of 277 ppm. No cross peaks are observed for the N3 and N15 sites for which there is not a directly attached hydrogen atom. Peak intensity in a ^{14}N-^{1}H HMQC MAS NMR spectrum depends on the recoupling of ^{14}N-^{1}H dipolar couplings, here using the phase-inverted R^3 method.[19,22,78-81] Figure S3 in the Supporting Information compares the ^{14}N-^{1}H HMQC MAS NMR spectrum in Figure 1a to two other spectra recorded with different durations of R^3 recoupling of the ^{14}N-^{1}H dipolar couplings.

Considering the ^{1}H-^{15}N cross polarization (CP) MAS NMR spectrum in Figure 1b, note that in a CP MAS spectrum, the peak intensity depends on the transfer of transverse magnetisation from ^{1}H to ^{15}N during the CP contact time. The build-up of CP signal as a function of the contact time depends on the ^{1}H-^{15}N dipolar couplings that also determine the loss of signal due to $T_1\rho$ relaxation during the ^{1}H spin-lock pulse. Hence different build-up behaviour is observed for the protonated and non-protonated nitrogen resonances, i.e., CP MAS spectra are not quantitative. In Figure 1b, while the non-protonated N3 and N15 resonances are observed, it is evident that they have lower intensity than that is observed for the protonated N1, N7 and N10 resonances.

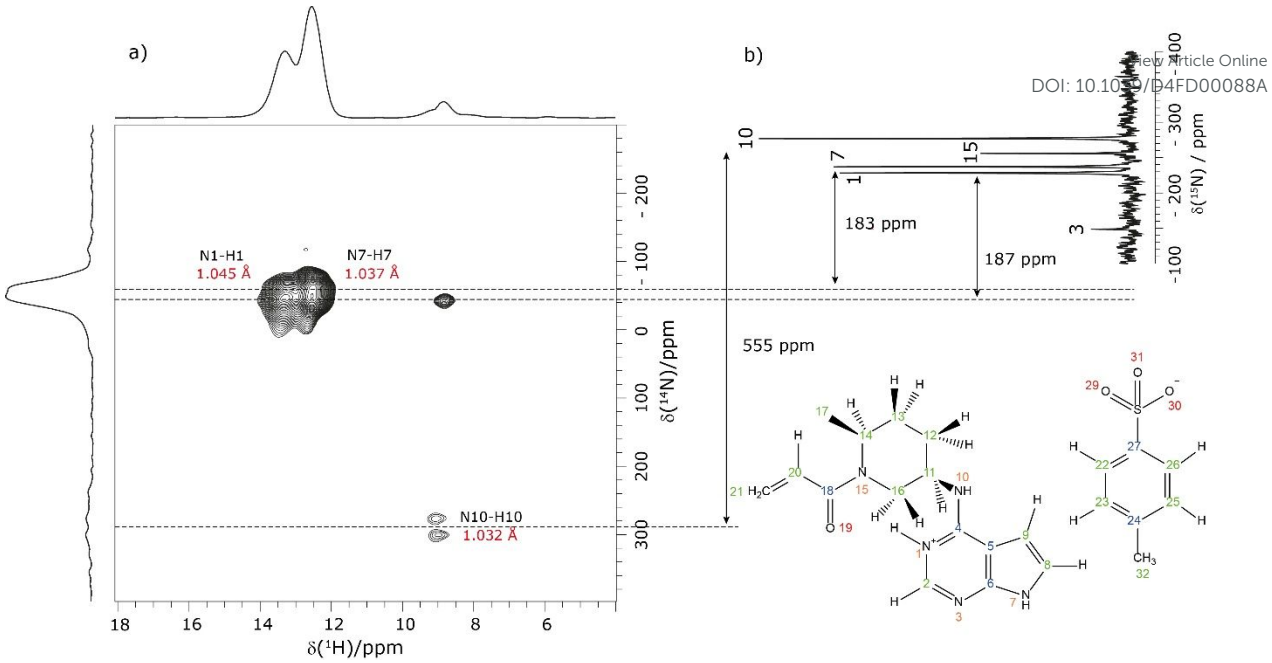

Figure 1: (a) A ^{14}N-^{1}H (600 MHz) HMQC MAS (60 kHz) NMR spectrum with skyline projections of **1** recorded with 16 rotor periods of phase-inverted R^3 recoupling, τ_{RCPL} = 267.2 μs. (b) Comparison to a 1D ^{1}H (500 MHz) – ^{15}N CP (3.5 ms) MAS (12.5 kHz) NMR spectrum of **1** acquired with 10,240 co-added transients. The arrows indicate the difference between the ^{14}N shift and the ^{15}N chemical shifts for N1, N7 and N10.

Table 1: Experimentally determined ^{15}N chemical shifts and ^{14}N shifts (at a ^{14}N Larmor frequency of 43.3 MHz) of **1** from Figure 1, along with the GIPAW calculated parameters.

Atom No.	**$\delta(^{15}N)_{exp}$[a] (ppm)**	**$\delta(^{15}N)_{calc}$[b] (ppm)**	**$\delta(^{14}N)_{exp}$[c] (ppm)**	**$\delta^{Q}iso(^{14}N)_{exp}$[d] (ppm)**	**P_{Qexp}[e] (MHz)**	**P_{Qcalc}[f] (MHz)**
1	–228.3	–227.2	–46	183	2.6	–2.2
3	–148.8	–147.5	-	-	-	–4.0
7	–237.1	–227.3	–40	187	2.5	–2.1
10	–277.1	–278.3	277	555	3.8	–3.8
15	–256.1	–249.3	-	-	-	–4.2

[a] ^{15}N isotropic chemical shift values as taken from the ^{1}H-^{15}N CP MAS spectrum presented in Figure 1b.

[b] $\delta_{iso} = \sigma_{ref} - \sigma_{iso}$, where $\sigma_{ref} = -160$ ppm.

[c] Centre of gravity of the ^{14}N peaks extracted from the ^{14}N-^{1}H HMQC spectrum presented in Figure 1a. Here, the error is estimated to be within ±5 ppm.

[d] $\delta^{Q}iso(^{14}N)_{exp} = \delta(^{14}N)_{exp} - \delta(^{15}N)_{expt}$.

[e] P_{Qexp} is calculated from $\delta^{Q}_{iso}(^{14}N)_{exp}$ using the equation:

View Article Online
DOI: 10.1039/D4FD00088A

$\delta^{Q}_{iso} = (3/40)\ (P_Q/\nu_0)^2 \times\ 10^6$, where $P_Q = C_Q \sqrt{\left[1 + (n_Q^2/3)\right]}$.[19,21,99] Note that the sign of P_Q cannot be determined experimentally.

[f] DFT calculation for the geometry-optimised crystal structure of **1** (CCDC 2352028).

Table 2 lists the hydrogen bond parameters, namely the N…O and H…O distances as well as the NHO angles for the three intermolecular NH…O hydrogen bonds formed between the three NH moieties and oxygen atoms of the tosylate anion (see also Figure 2). Note that the H…O distances are the same (1.71 Å) for the N1-H1…O31 and the N1-H7…O31 hydrogen bonds formed by NH groups on two different API molecules with the same acceptor oxygen atom of one tosylate anion. Table 2 also compares the experimental and GIPAW calculated ^{1}H chemical shifts for the three NH groups in **1**. The NH GIPAW calculated ^{1}H chemical shifts are at least 0.7 ppm higher than the experimental ^{1}H chemical shifts. This is a consequence of the well-established temperature dependence of such hydrogen-bonded ^{1}H chemical shifts in both solution[100-103] and solid-state NMR,[14-17] whereby the ^{1}H chemical shift increases upon decreasing temperature, i.e., if the experimental measurement could be performed at close to 0 K, better agreement to the GIPAW calculation that corresponds to 0 K would be expected. In this regard, further note that the GIPAW calculated ^{1}H chemical shift is higher for H7 than for H1 (14.7 as compared to 14.1 ppm), while, experimentally, H1 has the higher ^{1}H chemical shift, noting the above discussion of the assignment based on the cross peak to N10 observed in Figure 1a.

View Article Online
DOI: 10.1039/D4FD00088A

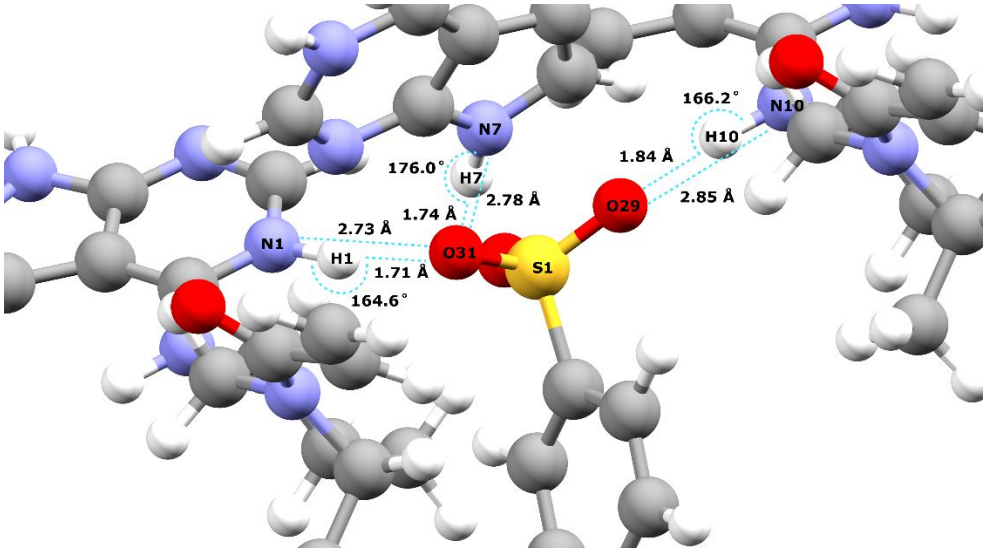

Figure 2: Intermolecular NH…O hydrogen bonds in the DFT (CASTEP) geometry optimised crystal structure of **1** (CCDC 2352028) between the Oxygen atoms of the tosylate salt and the three NH protons of the API free base (see Table 2 for the hydrogen bond distances and angles).

Table 2: Hydrogen bonding distances and angles from the geometry-optimised crystal structure of **1** (CCDC 2352028, see Figure 2) and experimental and GIPAW calculated ^{1}H NMR chemical shifts for the NH protons.

Atom 1	Atom 2	Atom 3	Distance [N…O] (Å)	Distance [H…O] (Å)	Angle [NHO] (°)	Expt. δ(^{1}H) (ppm)	Calc. δ(^{1}H) (ppm)
N10	H10	O29	2.85	1.84	166.2	9.2	9.9
N1	H1	O31	2.73	1.71	164.6	13.6	14.3
N7	H7	O31	2.78	1.71	176.0	12.8	14.7

In an NMR crystallography study of a pharmaceutical, further insight is obtained by carrying out a ^{1}H-^{1}H double-quantum (DQ) single-quantum (SQ) homonuclear correlation MAS NMR experiment, as presented for **1** in Figure 3 that was recorded at a ^{1}H Larmor frequency of 1 GHz. The creation of DQ coherence between two ^{1}H spins relies on a dipolar coupling between the two spins, with the dipolar coupling having an inverse cubed dependence on the internuclear distance: the presence or absence of DQ correlation peaks is indicative of the close proximity, typically up to 3.5 Å, or not of two hydrogen atoms.[97,104,105]

Consider the two highest ppm ^{1}H resonances at 12.8 and 13.6 ppm corresponding to the H7 and H1 NH, for which strong ^{14}N-^{1}H correlation peaks were observed in Figure 1. For the H7

SQ ^{1}H resonance, there is one pair of DQ peaks at 12.8 + 8.4 = 21.2 ppm, while for the H7 SQ ^{1}H resonance, there are two pairs of DQ peaks at 13.6 + 9.2 = 22.8 ppm and at 13.6 + 4.2 = 17.8 ppm. On the basis of the GIPAW calculation of ^{1}H chemical shifts for the geometry optimised crystal structure of **1**, these are assigned to intramolecular H-H proximities (see Table 3) of the NH H7 to the CH H8 neighbour in the same aromatic ring (at 8.4 ppm) and between the NH H1 and the CH H2 neighbour in the same aromatic ring (at 9.2 ppm) and between the NH H1 and the CH H11 of the adjacent ring (at 4.2 ppm).

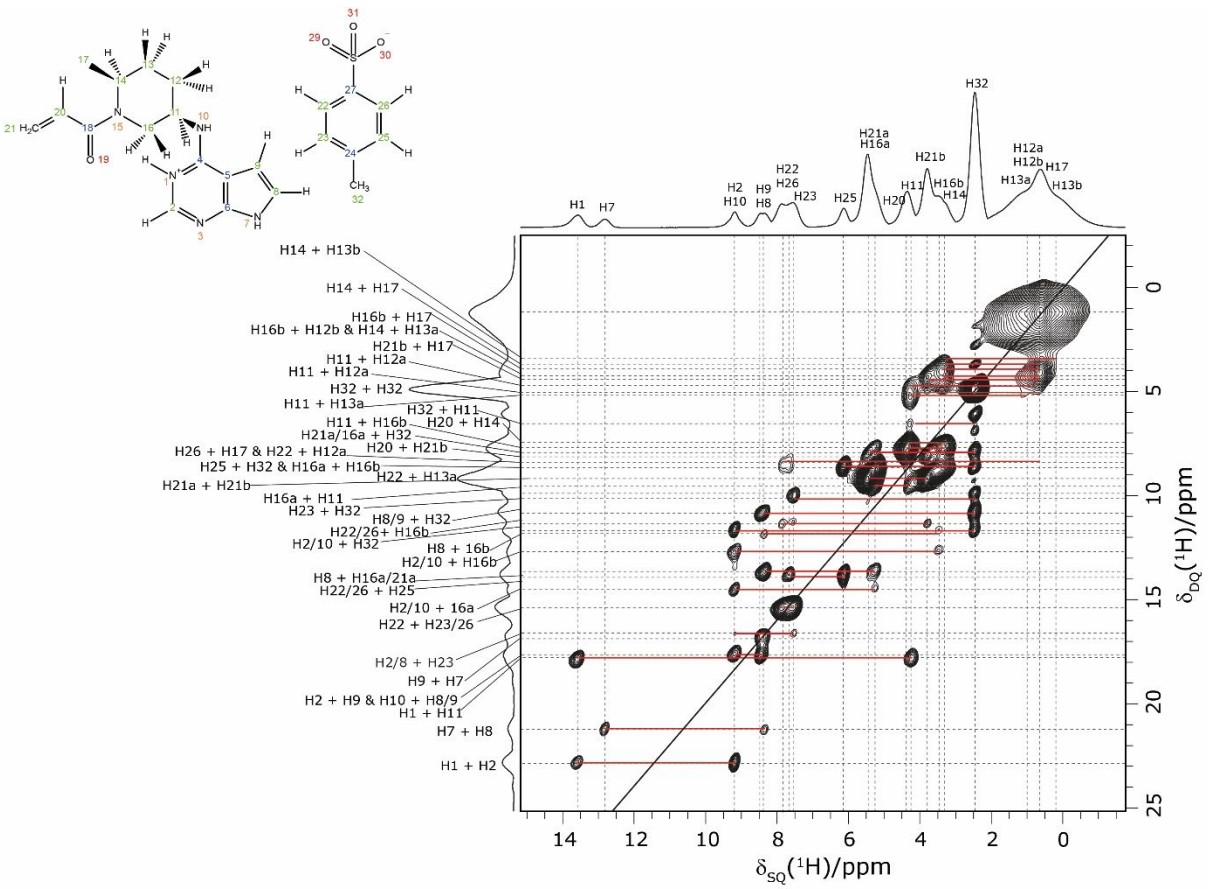

Figure 3: A ^{1}H (1 GHz) DQ-SQ 2D MAS (60 kHz) NMR spectrum of **1** with skyline projections recorded with one rotor period of BaBa recoupling. The base contour level is at 4% of the maximum peak height.

Table 3: H-H proximities (<3.5 Å) in **1** corresponding to experimentally observed ^{1}H DQ frequencies as seen in Figure 3.

Proton 1	δ_{SQ1} (ppm)	Proton 2	δ_{SQ2} (ppm)	δ_{DQ} (ppm)	Separation (Å)
13b (CH_3)	0.2	14 (CH)	3.3	3.5	2.49
17 (CH_3)	0.6	14 (CH)	3.3	3.9	2.47, 2.47, 3.07
17 (CH_3)	0.6	16b (CH_2)	3.5	4.1	2.42, 3.31
12b (CH_2)	0.7	16b (CH_2)	3.5	4.2	2.65

13a (CH_2)	1.0	14 (CH)	3.3	4.3	2.36
17 (CH_3)	0.6	21b (CH_2)	3.8	4.4	2.47, 2.70
32 (CH_3)	2.4	32 (CH_3)	2.4	4.8	1.78, 1.78
12a (CH_2)	0.7	11 (CH)	4.3	5.0	2.50
12b (CH_2)	0.7	11 (CH)	4.3	5.0	3.07
13a (CH_2)	1.0	11 (CH)	4.3	5.3	2.49
32 (CH_3)	2.4	11 (CH)	4.3	6.7	2.97
16b (CH_2)	3.5	11 (CH)	4.3	7.8	3.05
14 (CH)	3.3	20 (CH)	4.4	7.7	1.88
32 (CH_3)	2.4	16a (CH_2)	5.3	7.7	3.21, 2.80, 2.64
32 (CH_3)	2.4	21a (CH_2)	5.4	7.8	3.16
21b (CH_2)	3.8	20 (CH)	4.4	8.2	2.43
26 (CH)	7.6	17 (CH_3)	0.6	8.4	2.77
32 (CH_3)	2.4	25 (CH)	6.2	8.6	2.53, 3.00
12a (CH_2)	0.7	22 (CH)	7.8	8.5	3.09
13a (CH_2)	1.0	22 (CH)	7.8	8.8	2.93
16a (CH_2)	5.3	16b (CH_2)	3.5	8.8	1.77
21b (CH_2)	3.8	21a (CH_2)	5.4	9.2	1.87
11 (CH)	4.3	16a (CH_2)	5.3	9.6	2.43
32 (CH_3)	2.4	23 (CH)	7.5	9.9	2.45, 3.31
32 (CH_3)	2.4	8 (CH)	8.4	10.8	2.90, 2.69
32 (CH_3)	2.4	9 (CH)	8.5	10.9	3.02, 2.96
26 (CH)	7.6	16b (CH_2)	3.5	11.1	2.70
32 (CH_3)	2.4	2 (CH)	9.2	11.6	2.63, 3.17
32 (CH_3)	2.4	10 (NH)	9.2	11.6	3.20, 3.34
16b (CH_2)	3.5	8 (CH)	8.4	11.9	2.63
16a (CH_2)	5.3	2 (CH)	9.2	14.5	2.90
16b (CH_2)	3.5	10 (NH)	9.2	12.7	2.31
11 (CH)	4.1	10 (NH)	9.1	13.2	2.95
16a (CH_2)	5.3	8 (CH)	8.4	13.7	2.17
25 (CH)	6.2	26 (CH)	7.6	13.8	2.48
21a (CH_2)	5.4	8 (CH)	8.4	13.8	3.43
25 (CH)	6.2	22 (CH)	7.8	14.0	2.71
16a (CH_2)	5.3	2 (CH)	9.2	14.5	2.90
16a (CH_2)	5.3	10 (NH)	9.2	14.5	2.71
23 (CH)	7.5	22 (CH)	7.8	15.3	2.49
26 (CH)	7.6	22 (CH)	7.8	15.4	2.71
8 (CH)	8.4	9 (CH)	8.5	16.9	2.70
11 (CH)	4.2	1 (NH)	13.6	17.9	2.13
9 (CH)	8.5	10 (NH)	9.2	17.7	2.56
9 (CH)	8.5	2 (CH)	9.2	17.7	3.18
8 (CH)	8.4	7 (NH)	12.8	21.2	2.51
2 (CH)	9.2	1 (NH)	13.6	22.8	2.25

[a]The proximities were extracted from the DFT geometry-optimised (CASTEP) crystal structure of **1** (CCDC 2352028).

The assignment of the CH ^{1}H resonances is aided by the two-dimensional ^{1}H-^{13}C heteronuclear correlation (HETCOR) solid-state NMR spectra of **1** presented in Figure 4b and 4c. These spectra were recorded using a pulse sequence whereby CP was employed to transfer magnetisation from ^{1}H to ^{13}C via ^{13}C-^{1}H heteronuclear dipolar couplings. Note that, for this experimental implementation at 60 kHz MAS and a ^{1}H Larmor frequency of 1 GHz, a low ^{13}C nutation frequency of 10 kHz was applied during CP such that the presented spectra had to be

separately recorded for the high-ppm (aromatic) and low-ppm (aliphatic) regions, as presented in Figure 4b and 4c, respectively. Figure 4 additionally presents in Figure 4a a one-dimensional ^{1}H (600 MHz)-^{13}C CP MAS (12.5 kHz) NMR spectrum of **1** that was recorded with a CP contact time of 2 ms. Asterisks in Figure 4a denote spinning sidebands that are observed at 83 ppm (corresponding to 12.5 kHz at the ^{13}C Larmor frequency of 150.9 MHz) away from the centreband for carbonyl, aromatic and alkene ^{13}C resonances that exhibit large chemical shift anisotropies.

The CP contact time was 500 μs for the one-dimensional ^{1}H-^{13}C CP MAS (12.5 kHz) NMR spectrum in Figure 4a and 2 ms for the 2D ^{1}H-^{13}C CP-HETCOR MAS NMR spectra in Figures 4b and 4c. As discussed above for the ^{1}H-^{15}N CP MAS NMR spectrum in Figure 1b, solid-state NMR spectra recorded using CP are not quantitative in that the peak intensities in the ^{1}H-^{13}C CP MAS NMR spectrum depend on the transfer of transverse magnetisation from ^{1}H to ^{13}C during the CP contact time. For the CP contact time of 500 μs as used to record the CP-HETCOR MAS NMR spectra, resonances are predominantly observed in Figure 4b and 4c for the protonated CH, CH_2 and CH_3 resonances. By comparison, for the CP contact time of 2 ms as used to record the one-dimensional CP MAS NMR spectrum in Figure 4a, similar intensity is observed for the protonated and non-protonated resonances.

In Figure 4, the results of the GIPAW calculation for the DFT (CASTEP) geometry-optimised crystal structure of **1** are represented by a stick spectrum in Figure 4a for the calculated ^{13}C chemical shifts and by black crosses in Figure 4b and 4c for the calculated ^{1}H and ^{13}C chemical shifts for the CH, CH_2 and CH_3 moieties. Table 4 lists the assigned experimental and GIPAW calculated ^{1}H and ^{13}C chemical shifts for **1**. For the aliphatic resonances, i.e., those with a ^{13}C chemical shift below 55 ppm, there is good agreement between solid-state NMR experiment and GIPAW calculation: for ^{13}C, the biggest discrepancy compared to experiment is for C14 at 2.0 ppm, while for ^{1}H, the biggest discrepancy is 0.4 ppm for H16b (see Figure 4a and 4c and Table 4). For the high ppm (> 100 ppm) ^{13}C resonances, the ^{1}H-^{13}C CP-HETCOR MAS NMR spectrum in Figure 4b enables the distinguishing of protonated and non-protonated carbon atoms for which the ^{13}C chemical shifts are similar, namely the C9 CH at 105.6 ppm from the C5 C at 102.3 ppm, as well as the C2 CH at 143.6 ppm from the C27 C at 141.8 ppm. Specifically, high intensity C9-H9 and C2-H2 cross peaks are observed for the directly bonded pairs of ^{13}C and ^{1}H at (105.6 ppm, 8.5 ppm) and (143.6 ppm, 9.2 ppm), respectively. By comparison, only weak intensity cross peaks are observed for proximities between the non-protonated C5 C at 102.3 ppm with H9 (at 8.5 ppm) that is attached to the neighbouring C9

atom of the 5-membered ring, and between the non-protonated tosylate C27 C at 141.8 ppm with H22 (at 7.8 ppm) and H26 (at 7.6 ppm) that are attached to the neighbouring C22 and C26 atoms of the phenyl ring.

The most crowded part of the ^{1}H-^{13}C CP-HETCOR MAS NMR spectrum in Figure 4b is between ^{13}C chemical shifts of 120 and 140 ppm corresponding to aromatic CH and alkene CH and CH_2 resonances. Moreover, this is where the greatest discrepancy between experiment and GIPAW calculation is observed. Considering ^{1}H chemical shifts below 6.5 ppm, four cross peaks are expected for the C25-H25 tosylate pair and the C20-H20, C21-H21a and C21-H21b alkene pairs. In Figure 4b, experimental cross peaks are observed for ^{13}C chemical shifts between 126.1ppm and 127.9 ppm for ^{1}H chemical shifts below 6.5 ppm, while the GIPAW calculated ^{13}C chemical shifts are 128.0, 136.5 and 135.8 ppm for C20, C21 and C25, respectively. For the assignment in Table 4, there is a discrepancy of 9.0 and 7.9 ppm for C21 and C25. The biggest discrepancy for ^{1}H is for the C8 CH, where the experimental and GIPAW calculated ^{1}H chemical shifts are 8.4 and 9.1 ppm, respectively.

Table 4 lists both solution (DMSO) and solid-state NMR chemical shifts for **1**. The differences between experimental solution- and solid-state NMR ^{13}C chemical shifts is mostly within ±2 ppm, as was the case for the discrepancy between most experimental solid-state and GIPAW calculated ^{13}C chemical shifts discussed above. The biggest difference between solid-state and solution ^{13}C chemical shifts is 4.6 ppm for C6. Greater variation as compared to the much smaller range of chemical shifts (~20 ppm for ^{1}H compared to ~200 ppm for ^{13}C) is observed for the ^{1}H chemical shifts, noting the greater sensitivity of the ^{1}H chemical shift to the solid-state packing, e.g., ring currents from the aromatic groups. Variations of more than 1 ppm are observed for the H9 CH and the H20 CH with solid-state and solution ^{1}H chemical shifts of 6.93 ppm and 8.5 ppm for H9 and 6.85 ppm and 4.4 ppm for H20.

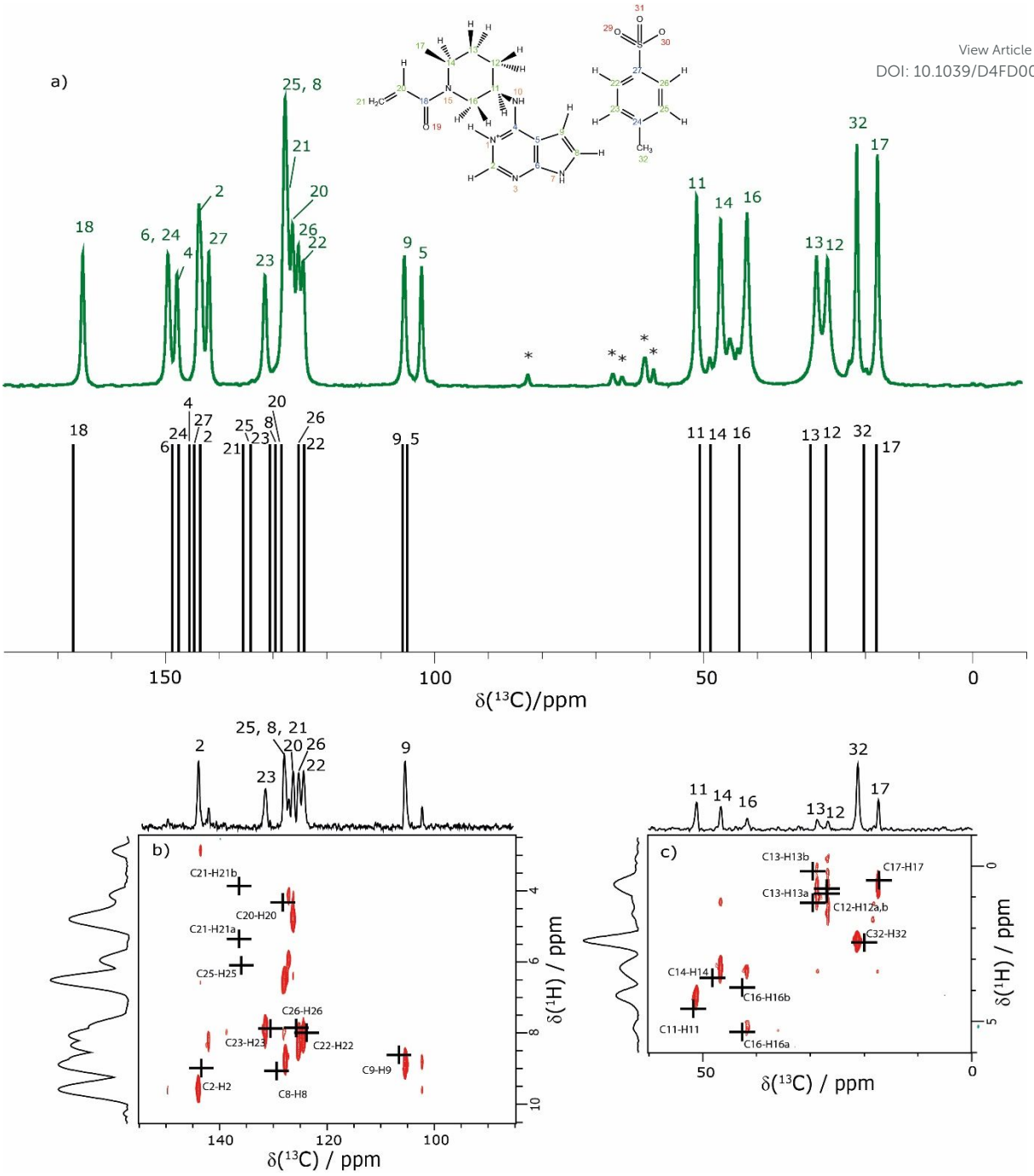

Figure 4. (a) A 1D ^{1}H (600 MHz)-^{13}C CP (2 ms) MAS (12.5 kHz) NMR spectrum of **1** acquired with 2,048 co-added transients. The asterisks denote spinning sidebands. The stick spectrum represents the GIPAW calculated ^{13}C chemical shifts for the DFT (CASTEP) geometry-optimised structure of **1** (CCDC 2352028, see Table 4). (b) and (c) Two-dimensional ^{1}H (1 GHz)-^{13}C CP (500 μs) HETCOR MAS (60 kHz) NMR spectra with skyline projections for the aromatic and aliphatic regions, respectively. Here, the low-power ^{13}C irradiation during CP was at an irradiation frequency of (b) 120 ppm and (c) 50 ppm. The black crosses in (b) and (c) represent the GIPAW calculated chemical shifts for the directly bonded CH connectivities

up to 1.1 Å. The base contour level is at 17% and 14% of the maximum peak height for (b) and (c), respectively.

View Article Online
DOI: 10.1039/D4FD00088A

Table 4: Experimental solid-state and GIPAW calculated ^{1}H and ^{13}C NMR chemical shifts (in ppm) for **1**.

	Solution-State[a]		Solid-State		GIPAW Calculated[b]	
Atom No.	^{1}H	^{13}C	^{1}H	^{13}C	^{1}H	^{13}C
1 (NH^{+})	13.44	-	13.6	-	14.3	-
2 (CH)	8.39	142.7	9.2	143.6	9.0	143.6
4 (C)	-	149.9	-	147.9	-	145.8
5 (C)	-	101.7	-	102.3	-	105.6
6 (C)	-	145.0	-	149.5	-	148.4
7 (NH)	12.67	-	12.8	-	14.7	-
8 (CH)	7.44	124.4	8.4	127.9	9.1	129.7
9 (CH)	6.93	101.5	8.5	105.6	8.6	106.6
10 (NH)	9.19	-	9.2	-	9.9	-
11 (CH)	3.97 (4.00)	48.2 (48.9)	4.3	51.0	4.6	51.1
12 (CH_2)	1.96-1.80	24.7	0.7	26.6	0.9, 0.7	27.4
13 (CH_2)	1.80-1.61	28.8 (27.8)	1.0, 0.2	28.7	1.2, 0.2	29.8
14 (CH)	4.41 (4.81)	46.6 (42.3)	3.3	46.5	3.6	48.5
16 (CH_2)	4.54, 2.80 (4.11, 3.14)	39.3 (43.3)	5.3, 3.5	41.6	5.3, 3.9	42.9
17 (CH_3)	1.23 (1.16)	16.4 (14.9)	0.6	17.3	0.5[c]	17.4
18 (C=O)	-	165.0 (164.5)	-	165.4	-	166.5
20 (CH)	6.85	128.9 (128.7)	4.4	126.1	4.3	128.0
21 (CH_2)	6.12, 5.72 (6.12, 5.87)	127.2 (127.4)	5.4, 3.8	127.5	5.4, 3.8	136.5
22 (CH)	7.49	125.4	7.8	124.3	8.0	124.1
23 (CH)	7.12	128.0	7.5	131.6	7.8	131.1
24 (C)	-	145.4	-	149.6	-	147.8
25 (CH)	7.12	128.0	6.2	127.9	6.1	135.8
26 (CH)	7.49	125.4	7.6	125.3	7.8	125.6
27 (C)	-	137.6	-	141.8	-	144.8
32 (CH_3)	2.29	20.7	2.4	21.3	2.5[c]	20.0

[a] Solution-state data was measured in DMSO. (Brackets indicate chemical shifts for the trans rotamer around the amine bond.)

[b] GIPAW calculated values for the geometry-optimised crystal structure of **1** (CCDC 2352028). A reference shielding value of 172.0 ppm was used for all ^{13}C atoms above 45 ppm, whilst for the ^{13}C atoms below 45 ppm, a reference shielding value of 175.0 ppm was used.[90] In the case of ^{1}H, a reference value of 31 ppm was used.

[c] In the case of the methyl groups, an average value is reported for the ^{1}H GIPAW calculated chemical shifts.

Returning to the ^{1}H-^{1}H DQ-SQ MAS NMR spectrum of **1** that was presented in Figure 3, it is evident that the assignment of the ^{1}H SQ resonances in Figure 3 follows from the assignment of the CH correlation peaks in the ^{1}H-^{13}C CP-HETCOR MAS NMR spectra that were presented in Figure 4b and 4c. This is further shown in Figure 5 that presents the ^{1}H-^{13}C CP-HETCOR MAS NMR spectra (top) with the ^{1}H-^{1}H DQ-SQ MAS NMR spectra (bottom), whereby the HETCOR spectra have been rotated through 90° such that there is a common horizontal ^{1}H SQ chemical axis.

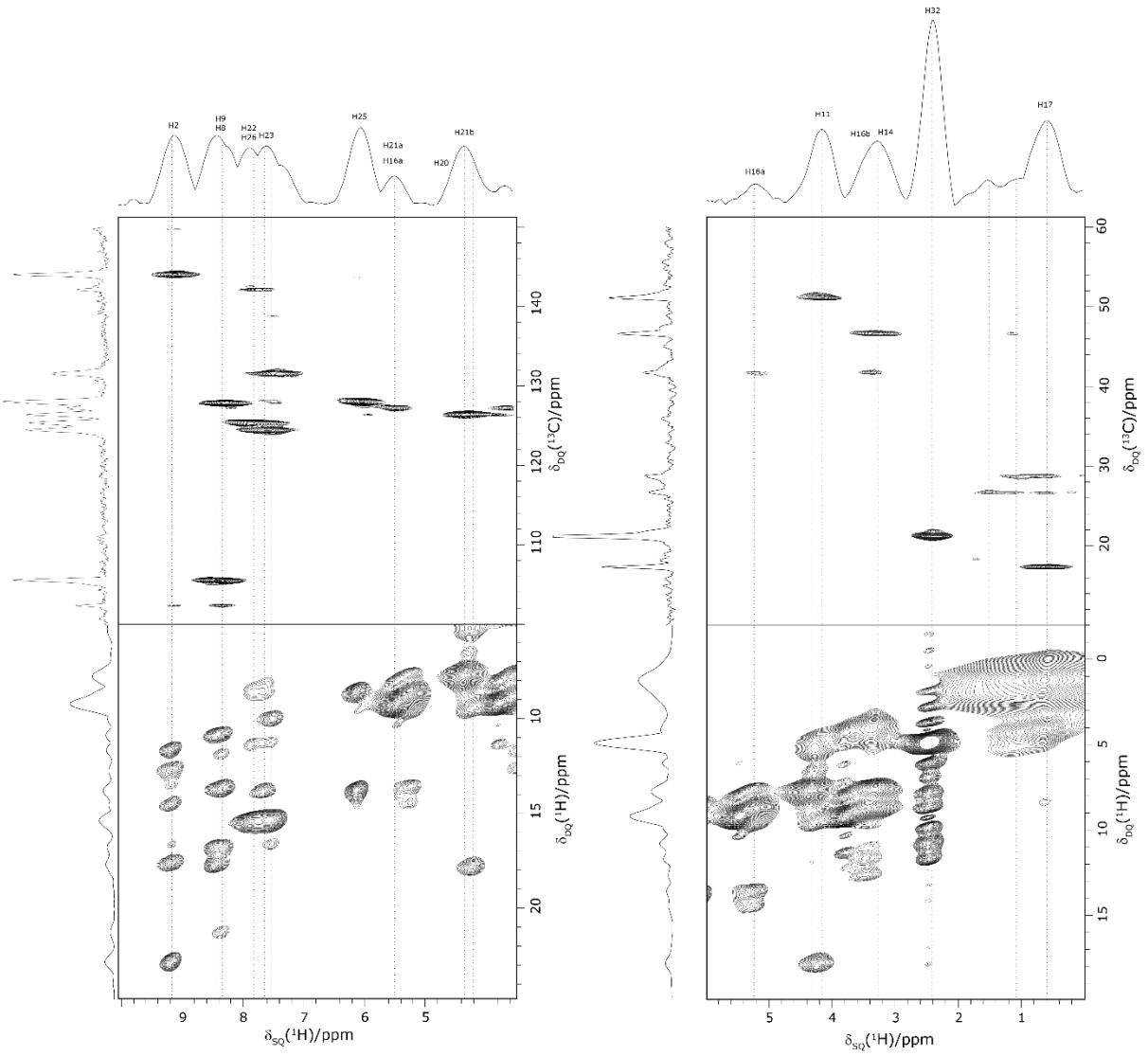

Figure 5. 2D MAS (60 kHz) NMR spectra with skyline projections of **1** recorded at 1 GHz. Top: ^{1}H-^{13}C CP HETCOR spectra for the high (left) and low (right) ppm regions repeated from Figure 4b and 4c, respectively. Bottom: Corresponding regions of the ^{1}H-^{1}H DQ-SQ spectrum repeated from Figure 3. Note that the ^{1}H-^{13}C CP HETCOR spectra have been rotated through 90° so as to achieve the alignment of the ^{1}H SQ axis as horizontal for both sets of spectra.

Case Study 2: Cellulose Polymorphs

In Ref. [5], Simmons et al. employed GIPAW calculation of ^{13}C NMR chemical shifts for 10 residue DFT-optimised molecular dynamics generated xylan structures to confirm that changes observed experimentally for the ^{13}C NMR chemical shifts for xylan are sensitive to the adoption of a two- and three-fold screw. As shown in Table 1 of Ref. [5], agreement between experiment and GIPAW calculation for the change in ^{13}C NMR chemical shift varied from within 0.8 ppm to within 3.4 ppm. In this context, we present here in Table 5, GIPAW calculated ^{13}C NMR chemical shifts for the crystal structures of cellulose Iα and cellulose Iβ,[106,107] noting that in both cases there are two distinct molecules in the asymmetric unit cell. Table 5 also compares the GIPAW calculations to experimental ^{13}C NMR chemical shifts reported by Brouwer and Mikolajewski.[108,109] While in most cases, agreement between experiment and GIPAW calculation is within 2 ppm, the C5 value for unit 2 in cellulose Iα exhibits a large discrepancy of 6.1 ppm. This discrepancy is significantly larger than for GIPAW calculations of mono- and disaccharides reported by Yates et al. for maltose,[29] by Brouwer et al. for glucose[110] and by Kibalchenko et al. for galactose.[111]

Table 5: Comparison of GIPAW calculated ^{13}C NMR chemical shifts (in ppm) for cellulose polymorphs to experiment.

	Cellulose Iα		Cellulose Iβ	
	GIPAW[a]	Expt[b]	GIPAW[a]	Expt[b]
Unit 1				
C1	107.6	105.6	106.6	106.1
C2	74.0	72.2	73.3	71.7
C3	74.4	74.6	73.2	75.3
C4	87.3	89.4	87.9	88.4
C5	70.8	73.1	71.0	71.4
C6	65.3	65.7	64.4	66.0
Unit 2				
C1	107.6	105.5	108.7	104.4
C2	75.4	71.2	70.7	71.7
C3	75.1	75.1	75.3	74.4
C4	93.6	90.3	85.7	89.2
C5	65.2	71.3	74.5	72.9

C6	63.3	65.8	65.3	65.2

[a] For the GIPAW calculated values, a reference shielding value of 168.1 ppm was used. The crystal structures for cellulose Iα (JINROO05, 792796)[106] and cellulose Iβ (JINROO01, 810597)[107] were used as starting points for geometry optimisation.

[b] Experimental values are taken from Brouwer and Mikolajewski.[108,109] Assignment to unit 1 and unit 2 is based on the relative change in the C5 ^{13}C chemical shift.

Summary and Outlook

This article has presented two case studies of the application of NMR crystallography of organic molecules to two important research areas, namely pharmaceuticals and plant cell walls. Building upon 20 years of literature applications, these two case studies showcase the great value of DFT calculation in complementing experimental solid-state NMR, with the GIPAW method. While agreement with experiment is good, indeed remarkably good given the inherent approximations of DFT, the discrepancy that typically corresponds to 1% of the chemical shift range for ^{1}H and ^{13}C is nevertheless restrictive, for example in seeking to provide evidence for different structural models for plant cell walls where there are only subtle changes in chemical shift. There is thus much motivation for continued innovation in the field of NMR crystallography.

Acknowledgements

ZR and JL thank EPSRC and Pfizer (ZR) and the University of Warwick and Bruker (JL) for PhD funding. The UK High-Field Solid-State NMR Facility used in this research was funded by EPSRC and BBSRC (EP/T015063/1) and, for the 1 GHz instrument, EP/R029946/1. We acknowledge the X-ray diffraction and the Scientific Computing Research Technology Platform at the University of Warwick for the PXRD experiment and for cellulose CASTEP calculations, respectively. Helpful discussions with Anjali Menakath, Ben Tatman and Mohammed Rahman at the University of Warwick are acknowledged. The calculated and experimental data for this study are provided as a supporting data set from WRAP, the Warwick Research Archive Portal at http://wrap.warwick.ac.uk/***.

Supporting Information

Single-crystal X-ray diffraction of **1** (CCSC 2352028) details; Powder X-ray diffraction of **1**; Additional solid-state NMR spectra of **1**.

View Article Online
DOI: 10.1039/D4FD00088A

1. C. J. Pickard and F. Mauri, *Phys. Rev. B*, 2001, **63**, 245101.
2. J. R. Yates, C. J. Pickard and F. Mauri, *Phys. Rev. B*, 2007, **76**.
3. C. Bonhomme, C. Gervais, F. Babonneau, C. Coelho, F. Pourpoint, T. Azais, S. E. Ashbrook, J. M. Griffin, J. R. Yates, F. Mauri and C. J. Pickard, *Chem. Rev.*, 2012, **112**, 5733.
4. Z. Rehman, W. T. Franks, B. Nguyen, H. F. Schmidt, G. Scrivens and S. P. Brown, *J. Pharm. Sci.*, 2023, **112**, 1915.
5. T. J. Simmons, J. C. Mortimer, O. D. Bernardinelli, A. C. Poppler, S. P. Brown, E. R. Deazevedo, R. Dupree and P. Dupree, *Nat. Commun.*, 2016, **7**, 13902.
6. https://www.ccpnc.ac.uk/database/.
7. S. Sturniolo, T. F. G. Green, R. M. Hanson, M. Zilka, K. Refson, P. Hodgkinson, S. P. Brown and J. R. Yates, *Solid State Nucl. Magn. Reson.*, 2016, **78**, 64.
8. R. K. Harris, P. Hodgkinson, C. J. Pickard, J. R. Yates and V. Zorin, *Magn. Reson. Chem.*, 2007, **45**, S174.
9. P. Hodgkinson, *Prog. Nucl. Magn. Reson. Spectrosc.*, 2020, **118-119**, 10.
10. G. N. M. Reddy, D. S. Cook, D. Iuga, R. I. Walton, A. Marsh and S. P. Brown, *Solid State Nucl. Magn. Reson.*, 2015, **65**, 41.
11. H. Blade, C. D. Blundell, S. P. Brown, J. Carson, H. R. W. Dannatt, L. P. Hughes and A. K. Menakath, *J. Phys. Chem. A*, 2020, **124**, 8959.
12. M. Rahman, H. R. W. Dannatt, C. D. Blundell, L. P. Hughes, H. Blade, J. Carson, B. P. Tatman, S. T. Johnston and S. P. Brown, *J. Phys. Chem. A*, 2024, **128**, 1793.
13. E. K. Corlett, H. Blade, L. P. Hughes, P. J. Sidebottom, D. Walker, R. I. Walton and S. P. Brown, *Solid State Nucl. Magn. Reson.*, 2020, **108**, 101662.
14. S. K. Mann, M. K. Devgan, W. T. Franks, S. Huband, C. L. Chan, J. Griffith, D. Pugh, N. J. Brooks, T. Welton, T. N. Pham, L. L. McQueen, J. R. Lewandowski and S. P. Brown, *J. Phys. Chem. B*, 2020, **124**, 4975.
15. C. J. Pickard, E. Salager, G. Pintacuda, B. Elena and L. Emsley, *J. Am. Chem. Soc.*, 2007, **129**, 8932.
16. J. N. Dumez and C. J. Pickard, *J. Chem. Phys.*, 2009, **130**, 104701.
17. A. L. Webber, B. Elena, J. M. Griffin, J. R. Yates, T. N. Pham, F. Mauri, C. J. Pickard, A. M. Gil, R. Stein, A. Lesage, L. Emsley and S. P. Brown, *Phys. Chem. Chem. Phys.*, 2010, **12**, 6970.
18. S. Cavadini, S. Antonijevic, A. Lupulescu and G. Bodenhausen, *J. Magn. Reson.*, 2006, **182**, 168.
19. Z. H. Gan, J. P. Amoureux and J. Trebosc, *Chem. Phys. Lett.*, 2007, **435**, 163.
20. S. Cavadini, *Prog. Nucl. Magn. Reson. Spectrosc.*, 2010, **56**, 46.
21. A. S. Tatton, J. P. Bradley, D. Iuga and S. P. Brown, *Z. Phys. Chemie-Int. J. Res. Phys. Chem. Chem. Phys.*, 2012, **226**, 1187.
22. B. Tatman, H. Modha and S. P. Brown, *J. Magn. Reson.*, 2023, **352**, 107459.
23. F. Taulelle, *Solid State Sci.*, 2004, **6**, 1053.
24. R. K. Harris, *Solid State Sci.*, 2004, **6**, 1025.
25. R. K. Harris, *Analyst*, 2006, **131**, 351.
26. J. R. Yates, S. E. Dobbins, C. J. Pickard, F. Mauri, P. Y. Ghi and R. K. Harris, *Phys. Chem. Chem. Phys.*, 2005, **7**, 1402.
27. R. K. Harris, S. A. Joyce, C. J. Pickard, S. Cadars and L. Emsley, *Phys. Chem. Chem. Phys.*, 2006, **8**, 137.
28. C. Gervais, M. Profeta, V. Lafond, C. Bonhomme, T. Azais, H. Mutin, C. J. Pickard, F. Mauri and F. Babonneau, *Magn. Reson. Chem.*, 2004, **42**, 445.
29. J. R. Yates, T. N. Pham, C. J. Pickard, F. Mauri, A. M. Amado, A. M. Gil and S. P. Brown, *J. Am. Chem. Soc.*, 2005, **127**, 10216.
30. J. P. Bradley, S. P. Velaga, O. N. Antzutkin and S. P. Brown, *Cryst. Growth Des.*, 2011, **11**, 3463.
31. E. Salager, G. M. Day, R. S. Stein, C. J. Pickard, B. Elena and L. Emsley, *J. Am. Chem. Soc.*, 2010, **132**, 2564.

32. J. P. Bradley, C. J. Pickard, J. C. Burley, D. R. Martin, L. P. Hughes, S. D. Cosgrove and S. P. Brown, *J. Pharm. Sci.*, 2012, **101**, 1821.
33. A. S. Tatton, T. N. Pham, F. G. Vogt, D. Iuga, A. J. Edwards and S. P. Brown, *Crystengcomm*, 2012, **14**, 2654.
34. D. V. Dudenko, J. R. Yates, K. D. M. Harris and S. P. Brown, *Crystengcomm*, 2013, **15**, 8797.
35. J. D. Hartman, S. Monaco, B. Schatschneider and G. J. O. Beran, *J. Chem. Phys.*, 2015, **143**, 102809.
36. G. J. O. Beran, J. D. Hartman and Y. N. Heit, *Accounts Chem. Res.*, 2016, **49**, 2501.
37. J. D. Hartman, G. M. Day and G. J. O. Beran, *Cryst. Growth Des.*, 2016, **16**, 6479.
38. J. D. Hartman, R. A. Kudla, G. M. Day, L. J. Mueller and G. J. O. Beran, *Phys. Chem. Chem. Phys.*, 2016, **18**, 21686.
39. F. M. Paruzzo, A. Hofstetter, F. Musil, S. De, M. Ceriotti and L. Emsley, *Nat. Commun.*, 2018, **9**, 4501.
40. C. Guzman-Afonso, Y. L. Hong, H. Colaux, H. Iijima, A. Saitow, T. Fukumura, Y. Aoyama, S. Motoki, T. Oikawa, T. Yamazaki, K. Yonekura and Y. Nishiyama, *Nat. Commun.*, 2019, **10**.
41. K. Bartova, I. Cisarova, A. Lycka and M. Dracinsky, *Dyes Pigment.*, 2020, **178**, 8.
42. A. Scarperi, G. Barcaro, A. Pajzderska, F. Martini, E. Carignani and M. Geppi, *Molecules*, 2021, **26**, 14.
43. M. K. Dudek, J. Sniechowska, A. Wroblewska, S. Kazmierski and M. J. Potrzebowski, *Chem.-Eur. J.*, 2020, **26**, 13264.
44. M. Khalaji, P. Paluch, M. J. Potrzebowski and M. K. Dudek, *Solid State Nucl. Magn. Reson.*, 2022, **121**, 14.
45. T. Pawlak, I. Sudgen, G. Bujacz, D. Iuga, S. P. Brown and M. J. Potrzebowski, *Cryst. Growth Des.*, 2021, **21**, 3328.
46. R. Mathew, I. V. Sergeyev, F. Aussenac, L. Gkoura, M. Rosay and M. Baias, *Solid State Nucl. Magn. Reson.*, 2022, **119**, 101794.
47. D. H. Brouwer and J. G. Mikolajewski, *Solid State Nucl. Magn. Reson.*, 2023, **123**, 9.
48. J. H. Shen, V. Terskikh, J. Struppe, A. Hassan, M. Monette, I. Hung, Z. H. Gan, A. Brinkmann and G. Wu, *Chem. Sci.*, 2022, **13**, 2591.
49. D. Bernasconi, S. Bordignon, F. Rossi, E. Priola, C. Nervi, R. Gobetto, D. Voinovich, D. Hasa, N. T. Duong, Y. Nishiyama and M. R. Chierotti, *Cryst. Growth Des.*, 2020, **20**, 906.
50. F. Bravetti, S. Bordignon, E. Alig, D. Eisenbeil, L. Fink, C. Nervi, R. Gobetto, M. U. Schmidt and M. R. Chierotti, *Chem.-Eur. J.*, 2022, **28**, e202103589.
51. F. Bravetti, R. E. Russo, S. Bordignon, A. Gallo, F. Rossi, C. Nervi, R. Gobetto and M. R. Chierotti, *Molecules*, 2023, **28**, 1876.
52. F. Bravetti, L. Tapmeyer, K. Skorodumov, E. Alig, S. Habermehl, R. Huhn, S. Bordignon, A. Gallo, C. Nervi, M. R. Chierotti and M. U. Schmidt, *IUCrJ*, 2023, **10**, 448.
53. P. M. J. Szell, S. P. Brown, L. P. Hughes, H. Blade and S. O. N. Lill, *Chem. Commun.*, 2020, **56**, 14039.
54. P. M. J. Szell, J. R. Lewandowski, H. Blade, L. P. Hughes, S. O. N. Lill and S. P. Brown, *Crystengcomm*, 2021, **23**, 6859.
55. A. J. Al-Ani, P. M. J. Szell, Z. Rehman, H. Blade, H. P. Wheatcroft, L. P. Hughes, S. P. Brown and C. C. Wilson, *Cryst. Growth Des.*, 2022, **22**, 4696.
56. P. M. J. Szell, Z. Rehman, B. Tatman, L. P. Hughes, H. Blade and S. P. Brown, *ChemPhysChem*, 2023, **24**, 8.
57. M. Dracinsky, J. Vicha, K. Bartova and P. Hodgkinson, *ChemPhysChem*, 2020, **21**, 2075.
58. J. Blahut, J. R. Stocek, M. Sala and M. Dracinsky, *J. Magn. Reson.*, 2022, **345**, 107334.
59. J. R. Stocek, O. Socha, I. Cisarova, T. Slanina and M. Dracinsky, *J. Am. Chem. Soc.*, 2022, **144**, 7111.
60. A. P. Bartók and J. R. Yates, *J. Chem. Phys.*, 2019, **150**, 161101.

61. M. Dracinsky, *Molecules*, 2021, **26**, 3857.
62. T. V. Chaloupecka E, Bártová K, Nishiyama Y, Dracínský M, *Solid State Nucl. Magn. Reson.*, 2024, **130**, 101921.
63. M. Dracinsky, P. Unzueta and G. J. O. Beran, *Phys. Chem. Chem. Phys.*, 2019, **21**, 14992.
64. R. J. Iuliucci, J. D. Hartman and G. J. O. Beran, *J. Phys. Chem. A*, 2023, **127**, 2846.
65. S. T. Holmes, O. G. Engl, M. N. Srnec, J. D. Madura, R. Quinones, J. K. Harper, R. W. Schurko and R. J. Iuliucci, *J. Phys. Chem. A*, 2020, **124**, 3109.
66. S. T. Holmes, C. M. Boley, A. Dewicki, Z. T. Gardner, C. S. Vojvodin, R. J. Iuliucci and R. W. Schurko, *Magn. Reson. Chem.*, 2024, **62**, 179.
67. E. A. Engel, A. Anelli, A. Hofstetter, F. Paruzzo, L. Emsley and M. Ceriotti, *Phys. Chem. Chem. Phys.*, 2019, **21**, 23385.
68. M. Cordova, M. Balodis, B. S. de Almeida, M. Ceriotti and L. Emsley, *Sci. Adv.*, 2021, **7**, eabk2341.
69. M. Balodis, M. Cordova, A. Hofstetter, G. M. Day and L. Emsley, *J. Am. Chem. Soc.*, 2022, **144**, 7215.
70. M. Cordova, E. A. Engel, A. Stefaniuk, F. Paruzzo, A. Hofstetter, M. Ceriotti and L. Emsley, *J. Phys. Chem. C*, 2022, 11.
71. M. Cordova and L. Emsley, *J. Am. Chem. Soc.*, 2023, **145**, 16109.
72. M. Cordova, M. Balodis, A. Hofstetter, F. Paruzzo, S. O. N. Lill, E. S. E. Eriksson, P. Berruyer, B. S. de Almeida, M. J. Quayle, S. T. Norberg, A. S. Ankarberg, S. Schantz and L. Emsley, *Nat. Commun.*, 2021, **12**, 2964.
73. M. Cordova, P. Moutzouri, S. O. N. Lill, A. Cousen, M. Kearns, S. T. Norberg, A. S. Ankarberg, J. McCabe, A. C. Pinon, S. Schantz and L. Emsley, *Nat. Commun.*, 2023, **14**, 5138.
74. B. M. Fung, A. K. Khitrin and K. Ermolaev, *J. Magn. Reson.*, 2000, **142**, 97.
75. G. Metz, X. L. Wu and S. O. Smith, *J. Magn. Reson. Ser. A*, 1994, **110**, 219.
76. W. Sommer, J. Gottwald, D. E. Demco and H. W. Spiess, *J. Magn. Reson. Ser. A*, 1995, **113**, 131.
77. I. Schnell, A. Lupulescu, S. Hafner, D. E. Demco and H. W. Spiess, *J. Magn. Reson.*, 1998, **133**, 61.
78. D. P. Raleigh, M. H. Levitt and R. G. Griffin, *Chem. Phys. Lett.*, 1988, **146**, 71.
79. P. R. Costa, J. D. Gross, M. Hong and R. G. Griffin, *Chem. Phys. Lett.*, 1997, **280**, 95.
80. S. J. Huang, S. B. Liu and J. C. C. Chan, *Solid State Nucl. Magn. Reson.*, 2009, **36**, 110.
81. A. L. Webber, S. Masiero, S. Pieraccini, J. C. Burley, A. S. Tatton, D. Iuga, T. N. Pham, G. P. Spada and S. P. Brown, *J. Am. Chem. Soc.*, 2011, **133**, 19777.
82. S. Hayashi and K. Hayamizu, *Bull. Chem. Soc. Jpn.*, 1991, **64**, 685.
83. C. R. Morcombe and K. W. Zilm, *J. Magn. Reson.*, 2003, **162**, 479.
84. E. K. Corlett, H. Blade, L. P. Hughes, P. J. Sidebottom, D. Walker, R. I. Walton and S. P. Brown, *Crystengcomm*, 2019, **21**, 3502.
85. S. Hayashi and K. Hayamizu, *Bull. Chem. Soc. Jpn.*, 1991, **64**, 688.
86. R. K. Harris, E. D. Becker, S. M. C. De Menezes, P. Granger, R. E. Hoffman and K. W. Zilm, *Pure Appl. Chem.*, 2008, **80**, 59.
87. G. E. Martin and C. E. Hadden, *J. Nat. Prod.*, 2000, **63**, 543.
88. S. J. Clark, M. D. Segall, C. J. Pickard, P. J. Hasnip, M. J. Probert, K. Refson and M. C. Payne, *Z. Kristallog.*, 2005, **220**, 567.
89. J. P. Perdew, K. Burke and M. Ernzerhof, *Phys. Rev. Lett.*, 1996, **77**, 3865.
90. A. L. Webber, L. Emsley, R. M. Claramunt and S. P. Brown, *J. Phys. Chem. A*, 2010, **114**, 10435.
91. M. F. Brown, A. Casimiro-Garcia, Y. C. Che, J. W. Flanagan, M. E., A. M. Gilbert, M. M. Hayward, J. D. Langille, J. I. Montgomery, J.-B. Telliez, A. Thorarensen and R. J. Unwalla, *WO2015083028A1 Pyrrolo[2,3-d]pyrimidinyl, pyrrolo[2,3-b]pyrazinyl and pyrrolo[2,3-d]pyridinyl acrylamides*

https://patents.google.com/patent/WO2015083028A1/en?oq=WO2015%2f083028, 2015.

View Article Online
DOI: 10.1039/D4FD00088A

92. H. A. Ramírez-Marín and A. Tosti, *Drug Des. Dev. Ther.*, 2022, **16**, 363.
93. F. D'Amico, G. Fiorino, F. Furfaro, M. Allocca and S. Danese, *Expert Opin. Investig. Drugs*, 2018, **27**, 595.
94. H. Xu, M. I. Jesson, U. I. Seneyiratne, T. H. Lin, M. N. Shari, L. Xue, C. Nguyen, R. A. Everley, J. I. Trujillo, D. S. Johnson, G. R. Point, A. Thorarensen, L. Kilty and J. B. Telliez, *ACS Chem. Biol.*, 2019, **14**, 1235.
95. A. Thorarensen, M. E. Dowty, M. E. Banker, B. Juba, J. Jussif, T. Lin, F. Vincent, R. M. Czerwinski, A. Casimiro-Garcia, R. Unwalla, J. I. Trujillo, S. Liang, P. Balbo, Y. Che, A. M. Gilbert, M. F. Brown, M. Hayward, J. Montgomery, L. Leung, X. Yang, S. Soucy, M. Hegen, J. Coe, J. Langille, F. Vajdos, J. Chrencik and J. B. Telliez, *J. Med. Chem.*, 2017, **60**, 1971.
96. B. M. Samas, Y. Tao, D. J. Critcher, D. S. B. Daniels, K. P. Girard, G. S. Goeken and P. R. Rose, *US20210387989A1 Pyrrolo[2,3-d]pyrimidine tosylate salt, crystalline form thereof and manufacturing process and intermediates thereof*https://patents.google.com/patent/US20210387989A1/en 2021.
97. S. P. Brown, *Solid State Nucl. Magn. Reson.*, 2012, **41**, 1.
98. A. S. Tatton, T. N. Pham, F. G. Vogt, D. Iuga, A. J. Edwards and S. P. Brown, *Mol. Pharm.*, 2013, **10**, 999.
99. A. Samoson, *Chem. Phys. Lett.*, 1985, **119**, 29.
100. U. Liddel and N. F. Ramsey, *J. Chem. Phys.*, 1951, **19**, 1608.
101. J. T. Arnold and M. E. Packard, *J. Chem. Phys.*, 1951, **19**, 1608.
102. N. Muller and R. C. Reiter, *J. Chem. Phys.*, 1965, **42**, 3265.
103. M. Garcia-Viloca, R. Gelabert, A. González-Lafont, M. Moreno and J. M. Lluch, *J. Am. Chem. Soc.*, 1998, **120**, 10203.
104. S. P. Brown, *Prog. Nucl. Magn. Reson. Spectrosc.*, 2007, **50**, 199.
105. J. P. Bradley, C. Tripon, C. Filip and S. P. Brown, *Phys. Chem. Chem. Phys.*, 2009, **11**, 6941.
106. Y. Nishiyama, J. Sugiyama, H. Chanzy and P. Langan, *J. Am. Chem. Soc.*, 2003, **125**, 14300.
107. Y. Nishiyama, P. Langan and H. Chanzy, *J. Am. Chem. Soc.*, 2002, **124**, 9074.
108. D. H. Brouwer and J. G. Mikolajewski, *Cellulose*, 2023, **30**, 4827.
109. D. H. Brouwer and J. G. Mikolajewski, *Cellulose*, 2023, **30**, 11341.
110. D. H. Brouwer, K. P. Langendoen and Q. Ferrant, *Can. J. Chem.-Rev. Can. Chim.*, 2011, **89**, 737.
111. M. Kibalchenko, D. Lee, L. M. Shao, M. C. Payne, J. J. Titman and J. R. Yates, *Chem. Phys. Lett.*, 2010, **498**, 270.